ELSEVIER

Earth and Planetary Science Letters 204 (2002) 347–361

EPSL

www.elsevier.com/locate/epsl

The upper mantle transition zone discontinuities in the Pacific as determined by short-period array data

Sebastian Rost [a,*], Michael Weber [b,1]

[a] *Institut für Geophysik, Georg-August Universität Göttingen, Herzberger Landstrasse 180, D-37075 Göttingen, Germany*
[b] *GeoForschungZentrum Potsdam, Telegrafenberg E3, D-14473 Potsdam, Germany*

Received 20 May 2002; received in revised form 13 September 2002; accepted 18 September 2002

Abstract

Short-period array recordings from Pacific earthquakes show precursors to *PP* produced by underside reflections of *P*-waves off the discontinuities in the upper mantle. We use these events to study the structure of the transition zone discontinuities in the central and northern Pacific. The discontinuities of the mantle transition zone at depths of 410 km and 660 km are particularly interesting for the interpretation of the chemistry and temperature structure of the mantle transition zone. The *PP* reflections from these discontinuities are too small to be identified in unprocessed seismograms. Therefore, array methods are used to detect and identify the *PP* underside reflections. The data of several events show reflections from the 410-km discontinuity. The topography of the reflector can be used to study the olivine to spinel phase transition in the central and northwestern Pacific. The mean depth of the reflector is 404 ± 16 km with topography near the Hawaiian Islands and the Kuriles. Forward modeling enables an estimate of the minimum impedance contrast and the maximum thickness of the discontinuity. This study shows that the 410-km discontinuity must be sharper than 6 km, assuming a simple linear gradient for the $\alpha \rightarrow \beta$ phase change, with an impedance contrast of 8.9% as in IASP91, to be in agreement with our data. The minimum impedance contrast for a first-order discontinuity would be 6.5%. The 660-km discontinuity cannot be detected in this dataset using *PP* underside reflections in agreement with previous studies. Forward modeling shows that the non-detection of the 660 can be explained by a discontinuity with a thickness of more than 12 km for the IASP91 impedance contrast or by a first-order discontinuity with an impedance contrast of less than $\sim 9\%$.

Keywords: transition zone; mantle discontinuity topography; seismology

1. Introduction

Observations of reflected, refracted and converted phases from seismic discontinuities can be used to determine the layered structure of the Earth. Together with additional information from other disciplines of Earth sciences, the structure of the different discontinuities is used to model the chemistry, composition, mineralogy

* Corresponding author. Present address: Department of Earth Sciences, IGPP-CSIDE, University of California, 1156 High Street, Santa Cruz, CA, 95064, USA. Tel.: +1-831-459-1437; Fax: +1-831-459-3074.
E-mail addresses: srost@es.ucsc.edu (S. Rost), mhw@gfz-potsdam.de (M. Weber).

[1] Also at Universität Potsdam, Institut für Geowissenschaften, D-14476 Golm, Germany.

0012-821X/02/$ – see front matter © 2002 Elsevier Science B.V. All rights reserved.
PII: S0012-821X(02)00999-8

and thermal structure of the Earth, and may help to solve some of the important questions in mantle chemistry and dynamics.

Due to the importance of the upper mantle discontinuities to study the dynamics of the Earth, different techniques are used to explore the region below the Mohorovičić discontinuity down to depths of ~700 km. Conversions from *P*- to *S*-waves at the upper mantle discontinuities [1,2], receiver functions [3,4], reflections of *PP*- and *SS*-waves from the discontinuities [5–7] and *ScS* reverberations [8–10] have been used to determine the depth, the velocity and density contrast and the sharpness of the discontinuities, i.e. the depth interval over which the seismic parameters change. The discontinuities near 410 km and 660 km depth (hereinafter referred to as the 410 and the 660) are now a standard feature of almost all upper mantle velocity models, although the existence of the 660-km discontinuity for *P*-waves has been questioned recently [11,12]. For an overview on the present knowledge on the transition zone discontinuities see Helffrich [13].

This is a study of the 410 and the 660 along a corridor in the central Pacific using short-period waves. We study *PP* underside reflections off the discontinuities called P^dP, where *d* denotes the depth of the reflector. Earthquakes in the western and south–western Pacific rim are recorded at the short-period, small-aperture Yellowknife array (YKA). We use short-period array recordings to detect, identify and analyze these weak precursors. The use of *PP* reflections enables us to study the structure of the transition zone discontinuities in a region of the central Pacific where no sources or receivers are located. Additionally, short-period waves are able to resolve the topography on short scale lengths and can resolve the sharpness of the discontinuities.

We will present our data and the processing technique used to detect the low-amplitude *PP* precursors in the array recordings. We detect sev-

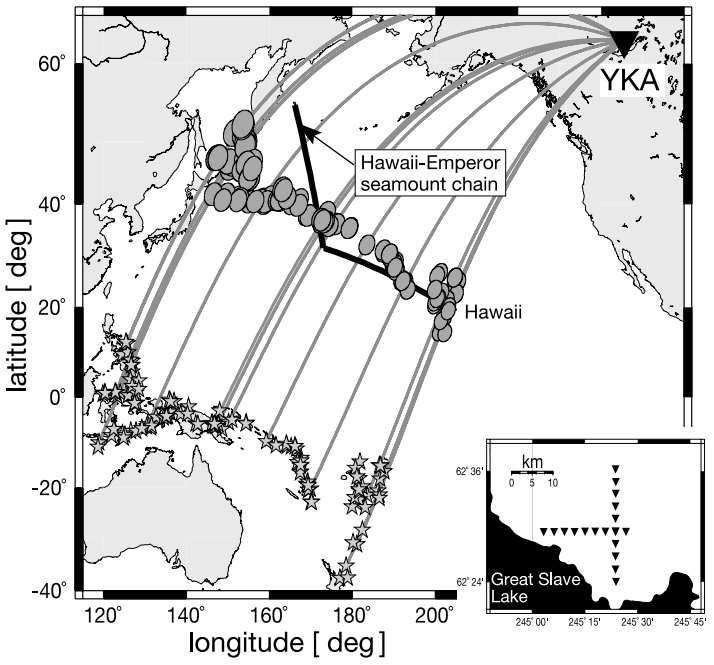

Fig. 1. Source receiver combination for this study. The 124 sources (stars) recorded at YKA (triangle) are located in the western Pacific rim. The *PP* surface reflection points (ellipses) form a corridor from the tip of the Hawaiian chain to the Kuril subduction zone. The first Fresnel zone, defined by the ±0.25s isochrone, is approximated by the center part of the saddle shaped *PP* Fresnel zone [20]. Great circle paths to YKA are marked as thin lines. The thick line shows the approximate location of the Hawaii–Emperor seamount chain. The insert shows the configuration of YKA, with two 20-km-long branches oriented West–East and South–North, equipped with nine short-period, vertical seismometers installed in vaults with a station spacing of 2.5 km.

eral reflections from the 410, but no signals originating from the 660. We use these results to specify limits on the impedance contrast and sharpness of the discontinuities and discuss our findings with respect to constraints from mineral-physics.

2. Data

The dataset used in this study consists of short-period recordings from the Canadian small-aperture, short-period YKA of events originating from the western and south–western Pacific rim (Fig. 1).

From the YKA data archive we chose events that show a signal-to-noise ratio (SNR) of *PP* to noise before the *P* onset better than 4 (in a band-pass filtered trace) and events with short *P* (or P_{diff}) coda. Large events are more likely to show P^dP above the noise level when the *P*-coda amplitude is small in the P^dP time window. An accurate measurement of PP–P^dP travel time differences is crucial for studying the discontinuities, but the *PP* onset is often buried in short-period data due to the interaction of *PP* with the crust at the reflection point. Clear *PP* arrivals reduce this source of error. Shallow events ($h \leq 100$ km) are preferred to avoid interference of P^dP and the depth phases (*pP* and *sP*).

In total, 124 out of ~1000 events from the appropriate source regions recorded at YKA between September 1989 and March 1997 satisfy these criteria and are shown in Fig. 1. The source receiver distance (Δ) for these events is 88–116° with backazimuths (θ) of 232–304°. The *PP* surface reflection points fill a corridor from the tip of the Hawaiian Islands to the Kuril subduction zone.

3. Processing

Due to the similar paths through the Earth, *PP* and P^dP arrive at the array with similar slownesses (Fig. 2). The slowness difference $\Delta u = u_{PP} - u_{P^dP}$ ($d = 410$, 660) in one-dimensional Earth models like IASP91 is smaller than 0.2 s/°.

Upperside reflections of the discontinuities near the source or receiver ($Pp_{410}p$ and $Pp_{660}p$) have similar travel times as P^dP in the epicentral distance range studied here, but show slownesses comparable to *P* (or P_{diff}). Phases asymmetrically scattered at the surface ($P_\Delta P$, where the *P*-wave is scattered at a distance Δ [14]) also arrive with similar travel times as P^dP and could be misinterpreted as P^dP [14–16]. These phases generally show lower or higher slownesses than *PP*, if the scattering volume is on the source or the receiver side, respectively. Therefore, to separate P^dP from the phases arriving with similar travel times a robust determination of the slowness is necessary. For identification of P^dP we chose the following three criteria:

1. *Slowness*. A slowness similar to *PP* (at most 0.2 s/° smaller than *PP*) is required to identify a phase as P^dP. The P^dP slowness is much larger than the slowness of Pp_dp and $P_\Delta P$ and can be used to discriminate between these phases.
2. *Backazimuth*. We require backazimuths along the great-circle path to rule out asymmetric reflections off the great-circle path, that have a source different from P^dP. This criterion also

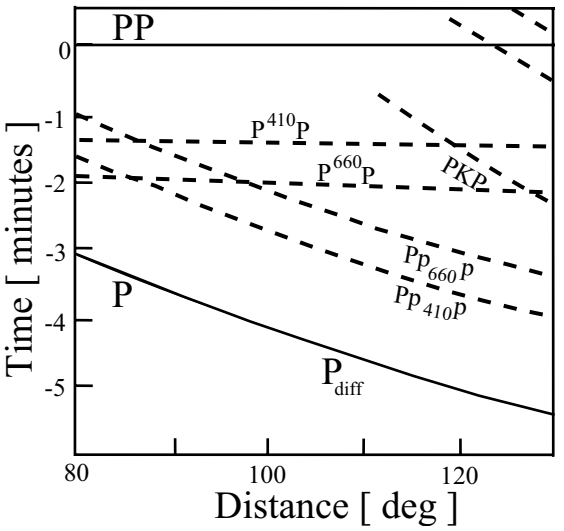

Fig. 2. *P*-wave travel time curves computed for IASP91 for epicentral distances of 80–130°. Travel times are relative to the *PP* arrival. Phases with slowness similar to *PP* (such as the underside reflections P^dP) are nearly parallel to *PP*. Phases like *P* and the upperside reflections off the discontinuities (P_{p410p} and P_{p660p}) show much smaller slownesses.

ensures that coherent phases from other possible sources (second event within the time window or near receiver quarry blasts) can be identified.

3. *Coherence*. P^dP is a coherent phase across the array. Noise might show by chance slowness and backazimuth of P^dP but is, as a statistical signal, not coherent.

Fig. 3 shows 4th-root vespagrams [17] of four events showing phases which could be identified as $P^{410}P$. The phases show different amplitudes, but all show slownesses similar to *PP*. Vespagrams require the input of a fixed backazimuth for their calculation and cannot be used to study all the criteria required for a detection of P^dP. Therefore, we use frequency–wavenumber analysis (fk-analysis) [18,19] to determine slowness, backazimuth and coherence needed to identify P^dP. The fk-analysis calculates the frequency–wavenumber power spectrum, that describes the power distributed among different wave velocities and directions of approach. This means we measure the complete slowness vector for an arriving phase. We separate the slowness vector into horizontal slowness u and backazimuth θ. Most array methods use the differential time delays of a signal recorded at the array stations [20]. The time delay required to bring the signals into phase provides a direct estimate of u and θ of the signal. The fk-analysis performs a grid search for all u and θ combinations to find the best parameter combination that produces the highest amplitudes for the summed signal. The calculation is performed in the spectral domain to save computation time

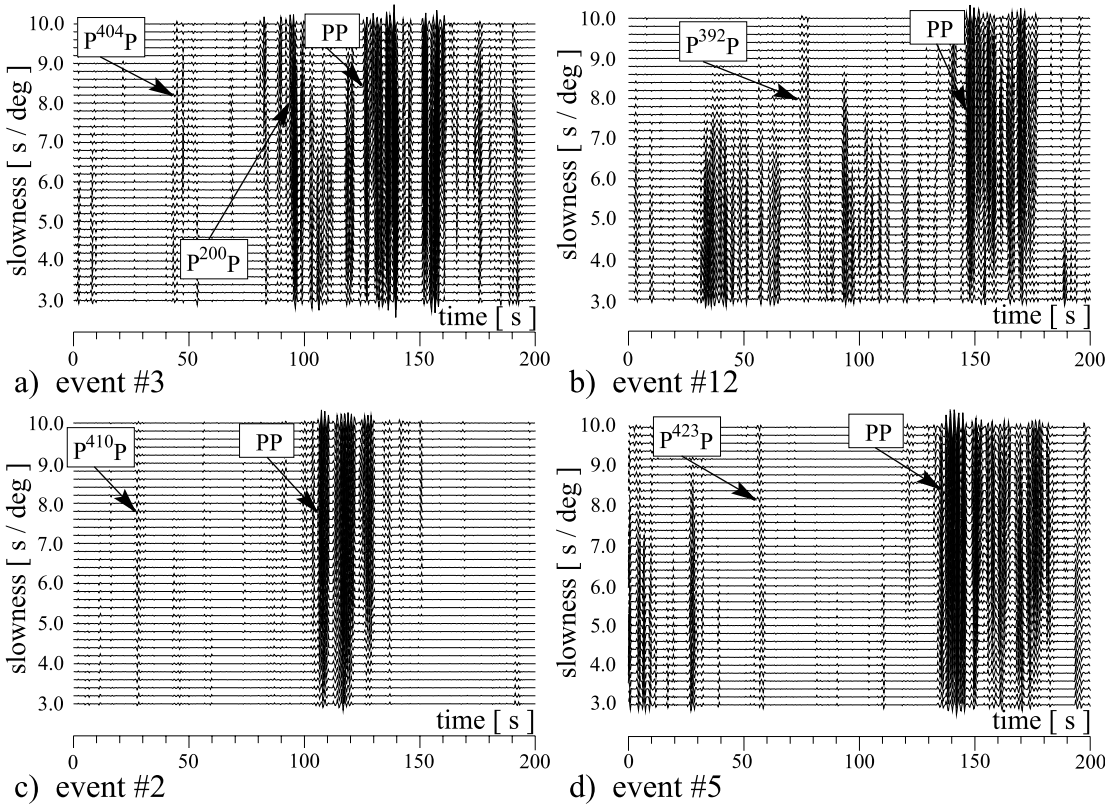

Fig. 3. Fourth-root vespagrams of four events. The events show phases with correct slowness to be interpreted as P^dP. (a) Vespagram for event 3 (see Table 1). The additional phase between $P^{404}P$ and *PP* is identified as $P^{200}P$ as described in [20]. (b) Same as (a) for event 12. The strong phases before and after $P^{392}P$ with smaller slownesses are *pP* and *sP*. (c) Event 2 shows only a weak $P^{410}P$ onset. (d) The strong phase in event 5∼30 s before $P^{423}P$ is asymmetrically scattered energy or an upperside reflection ($Pp_{660}p$) off the 660.

[18,21,22]. The fk-analysis is applied to the raw unprocessed array seismograms, but uses only the frequencies between 0.5 and 1.4 Hz in the transformation into the frequency domain. The result of the fk-analysis is displayed as a fk-diagram, that shows the power spectral density as function of slowness and backazimuth in a polar-coordinate system.

To identify a phase as P^dP we demand slowness deviations from the theoretical values to be smaller than $u_{P^dP} \pm 0.5$ s/° and backazimuth deviations of $\theta_{P^dP} \pm 15°$. The allowed slowness range for the detection of P^dP is slightly larger than the maximum deviation of u_{P^dP} from u_{PP}, because u_{P^dP} is influenced by noise and u cannot be measured with a higher precision. The coherence of the signal is studied qualitatively by comparing the result of the fk-diagram with the theoretical array–response function (ARF) of YKA [18]. The ARF is the response of the array to a 1-Hz signal arriving with $u = 0$ s/° and is controlled solely by the design (aperture, configuration and interstation spacing) of the array. For YKA the ARF is symmetric and cross-shaped [20]. The fk-analysis must be applied to short time windows to guarantee unambiguous results, therefore, the fk-analysis cannot be applied to the complete time window between P and PP where the P^dP phases are expected to arrive. To study the development of u and θ over a period of time, the sliding-window fk-analysis is used to study P^dP [20,23]. For the sliding-window fk-analysis a short time window of constant width is shifted along the seismogram with a constant step size, and a standard fk-analysis is performed at each step. The sliding-window fk-analysis transfers the array seismograms into coherence time series for slowness, backazimuth and coherence. The sliding-window fk-analysis allows the search for P^dP phases in numerous time windows, and not only in time windows where underside reflections from well established discontinuities are expected. It is best displayed as a series of fk-diagrams called a fk-movie [20] and examples can be seen at: http://www.uni-geophys.gwdg.de/~srost/fk-movies.htm.

Following earlier studies of PP using YKA [20] we use a window width of 4 s and a step size of 1 s to detect P^dP. We use rectangular time windows for the fk-analysis, but tapered windows have been tested and show no difference to the simple untapered windows.

Different tests for the slowness and backazimuth resolution show that the fk-analysis applied to YKA data is able to resolve the slowness difference between P^dP and Pp_dp. The minimum resolvable slowness difference, even when the sig-

Table 1
Events showing a reflector between 330 and 430 km

#	Origin	Time	Lat (°)	Lon (°)	h (km)	m_b	Δ (°)	Δt_{410} (s)	d (km)	Δd (km)
1	10-dec-1990	09:34	−5.947	142.250	20.5	5.8	101.3	80.5	396	8
2	08-jan-1991	22:04	−18.123	−173.333	38.0	6.0	92.6	81.1	410	8
3	04-jun-1993	10:49	3.787	128.502	26.4	5.7	98.8	81.3	404	8
4	09-dec-1993	04:32	0.596	125.990	31.0	6.5	102.7	83.9	415	8
5	27-apr-1994	09:23	−21.524	−173.539	33.2	6.2	95.8	83.7	423	8
6	08-oct-1994	21:44	−1.255	128.021	14.1	6.4	103.5	83.7	413	8
7	27-jan-1995	20:16	−4.546	134.461	20.2	6.2	103.5	80.7	394	8
8	19-mar-1995	23:53	−4.345	135.126	32.3	6.2	103.0	83.8	415	8
9	21-apr-1995	00:09	12.085	125.632	25.9	6.2	92.4	67.4	330	10
10	28-feb-1996	09:44	1.753	126.041	116.0	6.2	101.6	75.4	366	8
11	20-jul-1996	07:41	−19.797	−177.569	362.2	5.7	95.8	84.4	427	8
12	05-aug-1996	22:38	−20.713	−178.235	555.0	6.4	96.7	79.1	392	8
13	05-nov-1996	09:41	−31.180	−179.833	355.0	5.9	106.7	81.0	393	8

The following parameters are given: event number (#), event origin date and time, event latitude (Lat) and longitude (Lon), source–receiver distance (Δ), event depth (h), event magnitude (m_b), PP–$P^{410}P$ differential travel time ($\Delta t_{410} = t_{PP} - t_{P^{410}P}$), reflector depth ($d$), estimated reflector depth error (Δd). Event locations are from Engdahl et al. [51]. The depth of the reflector was computed using IASP91.

nals show only small travel time differences, is about 0.2 s/° and the backazimuth resolution is about 10°. For more resolution tests see [20,23].

An application of the sliding-window fk-analysis on real data (event 3 in Table 1) is given in Fig. 4. Fig. 4a displays the beam trace of YKA for reference. *P* (Fig. 4b) and *PP* (Fig. 4c) are detected as coherent phases, due to the resemblance of the fk-diagram with the ARF, with correct slowness and backazimuth. The time windows matching the travel times for $P^{660}P$ and $P^{410}P$ (Fig. 4d and e, respectively) show a coher-

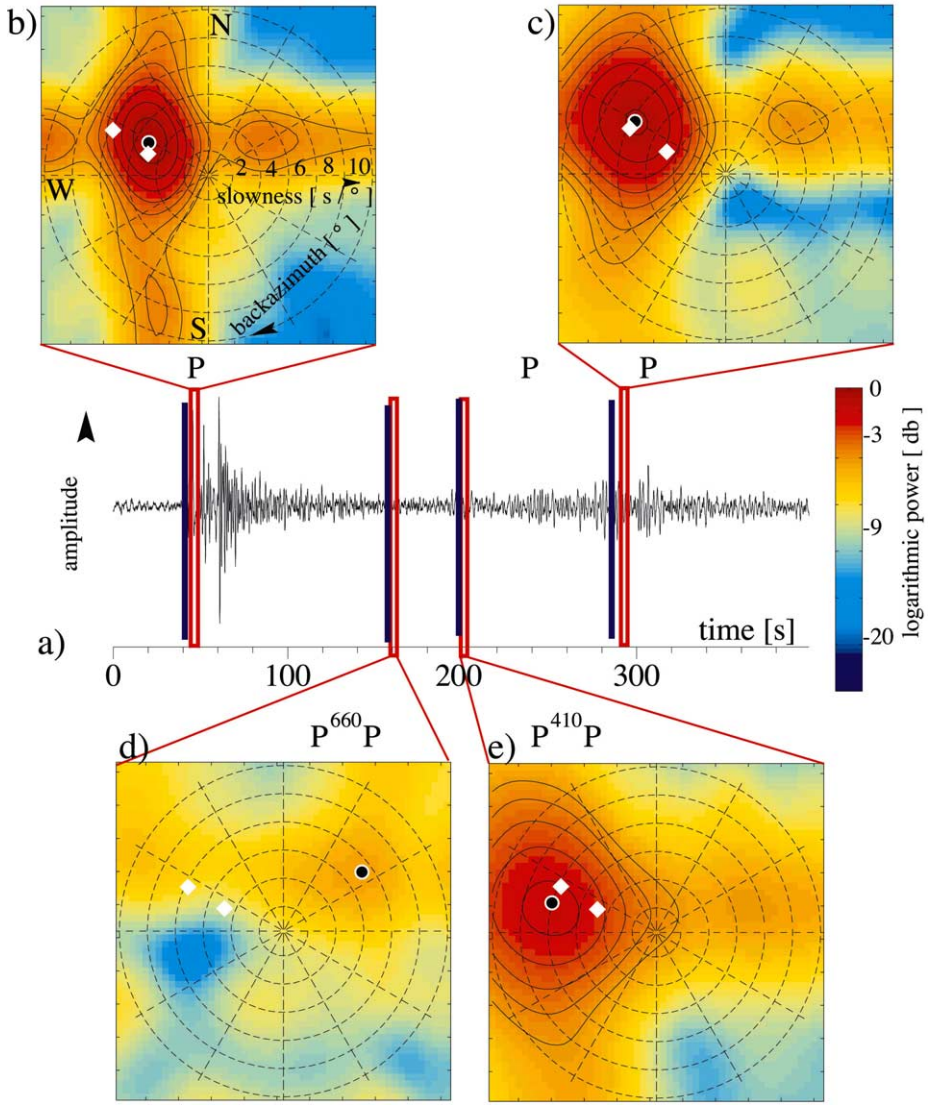

Fig. 4. Sliding-window fk-analysis snapshots for event 3. (a) Beam trace of YKA using the theoretical slowness and backazimuth of *PP*. IASP91 theoretical arrival times of *P*, *PP*, $P^{660}P$ and $P^{410}P$ are marked by vertical blue lines. Red frames mark time windows used for the fk-diagrams shown in (b)–(e). (b) fk-diagram of *P* time window ($u_P^{theo} = 4.43$ s/°). The theoretical parameters (slowness and backazimuth) of *P* and *PP* for IASP are marked by the white diamonds. The black circle marks the observed slowness and backazimuth. (c) *PP* arrival showing the expected high slowness ($u_{PP}^{theo} = 7.65$ s/°). (d,e) Time windows of $P^{660}P$ and $P^{410}P$, respectively. No coherent signal is visible for the $P^{660}P$ time window, whereas $P^{410}P$ shows a coherent phase arriving with *PP* slowness and along the great circle path.

ent signal and appropriate slowness and backazimuth only for $P^{410}P$. The time window for $P^{660}P$ shows no coherent onset and contains little energy.

$P^{410}P$ meets the three criteria used to identify P^dP. The PP–$P^{410}P$ differential travel time can be converted to a reflector depth of 404 km using the IASP91 model. We use the middle of the first 4-s fk-window that shows a clear P^dP phase in the sliding-window fk-analysis as a reference point to measure the travel time. Because short-period data often show gradual PP onsets due to crustal structure at the reflection point, the identification of the PP arrival is often difficult. To detect the PP onset we search for the highest energy of the fk-analysis in a ± 5-s time window around the IASP91 theoretical onset of PP. The ± 5-s time window is short enough to exclude the large amplitude P^wP phases, the reflection at the free water–air boundary at the PP midpoint after traveling through the oceanic water. This measurement is very rough since we cannot be sure to detect the correct PP onset and accounts for the large picking error of ± 2 s, as discussed in more detail later. Because the P^dP phases show very small amplitudes, normally only the strongest part of the signal is visible in the sliding-window fk-analysis; the P^dP detections are only visible for 3–4 s.

4. Results

4.1. Detected discontinuity: 410-km discontinuity

The sliding-window fk-analysis has been applied to a time window ~ 10 s before P to ~ 30 s after PP of the 124 events selected from the YKA dataset (Fig. 1). Phases that are identified as P^dP can be found in three different depth bands around 410 km, 200 km [20] and 60–100 km. We find 13 out of 124 events that show reflections at depths near 410 km with depths from ~ 330 to ~ 430 km (Table 1). The depths of the reflector given in Table 1 depend strongly on the model used to convert the differential travel time to depth. We use the one-dimensional Earth model IASP91 and do not correct for possible three-dimensional velocity structure as seen in tomographic models of the upper mantle. The size of these possible variations in the study area is discussed below. Different reasons for the large number of non-detections of $P^{410}P$ are plausible. Synthetic tests show that PP underside reflections have amplitudes of about 5% of PP and their detection in the P-coda is difficult. P^dP might be overprinted by other phases such as pP, sP and Pp_dp and their coda. Unfavorable radiation patterns of the source could also influence the P^dP amplitudes. Events showing P^dP and events without P^dP detections have been checked for any correlation with source location, source depth or magnitude, but no correlation was found. In some cases the signal generated noise level in the precursor time window is small, which should allow the detection of P^dP, but often no precursors are detected. Topography on the discontinuity influences especially the underside reflections of short-period waves through focusing and defocusing of the wavefield [24], and could result in strongly reduced P^dP amplitudes and sparse detections of P^dP. Short-period PP underside reflections are very sensitive to the thickness of the discontinuity, i.e. the transition where the material properties change. A change of this thickness by temperature or compositional variations might account for the non-detections as proposed by Chevrot et al. [2] and is discussed in more detail later. Using ScS reverberations [9,25] it has been noticed that the 410 shows a broad range of shear reflectivity [26]. The areas where we detect $P^{410}P$ reflections could be areas of the 410 with high P reflectivity due to thickness variations or small-scale topography of the discontinuity. No final answer on the reason for the large amount of non-detections can be given.

The PP–$P^{410}P$ travel time differences given in Table 1 are converted to reflector depth d using ray tracing methods and the one-dimensional Earth model IASP91 [27]. It has been suggested that short-wavelength topography could cause significant errors in estimates of discontinuity depth [28], but this effect should not bias the topography measured using short-period data to the same extent due to the much smaller Fresnel zones. The Fresnel zone of PP is not compact

since *PP* is a minimax phase. The Fresnel zone is saddle shaped and extends to very long distances from the ray-theoretical *PP* reflection point. The ellipses shown in Fig. 1 approximate only the central part of the first Fresnel zone [20]. The extended Fresnel zones might potentially alias distant structure to the bounce point and a final statement on the effect of the *PP* Fresnel zones on the resolution of the short-period waves is difficult. Nonetheless, the short-period data are more sensitive to the focusing and the defocusing effects of the topography and to asymmetric reflections at dipping interfaces [29]. The column Δd in Table 1 gives the estimated error of the depth location due to the combined *PP* and $P^{410}P$ picking error of $\sim$2 s. This large picking error is due to the use of the center of the 4-s time window of the fk-analysis as the reference point for P^dP and uncertainty in the *PP* arrival time. Using $PP–P^dP$ differential travel times greatly mitigates the effects of hypocentral uncertainties and lateral variations in crustal and upper mantle structure so that these do not influence our measurements.

Since we use *PP* as a reference phase the apparent discontinuity depth depends upon the velocity in the upper mantle above the discontinuities. Slower velocities relative to the reference model would result in greater apparent depth. Thus lateral heterogeneity in the upper mantle will introduce errors into the computed discontinuity depth. The surface reflection points are located in regions where the lithosphere is older than 110 Myr [30]. It has been shown that *PP–P* differential travel times, sensitive to velocity variations of the upper mantle, decrease with age of the lithosphere [31], with 0–1 s variation for lithosphere older than 100 Myr. The region of the Pacific studied here shows only very small variations of the *PP–P* differential travel times, indicating only small amplitude lateral heterogeneities on large scale lengths in the region. For the determination of *PP–P* differential travel times long-period waves are used that are not as sensitive to small-scale upper mantle heterogeneity as the short-period data used here [31]. Nonetheless, Woodward and Master's study [31] shows that old oceanic lithosphere has little heterogeneity on large scale lengths. Due to the lack of appropriate upper mantle short-scale tomography studies in the northern Pacific we have to use this long-period study and assume that the errors due to lateral heterogeneity are less than 1 s, i.e. less than $\sim$5 km between different reflection points. Due to the lack of knowledge about the short-scale structure in the upper mantle in the region studied we do not correct for this error. A global study of converted *Pds* phases shows evidence that the depth of the transition zone discontinuities is correlated with lateral *P* and *S* velocity variations in the uppermost mantle as revealed by tomographic studies [2]. Nonetheless,

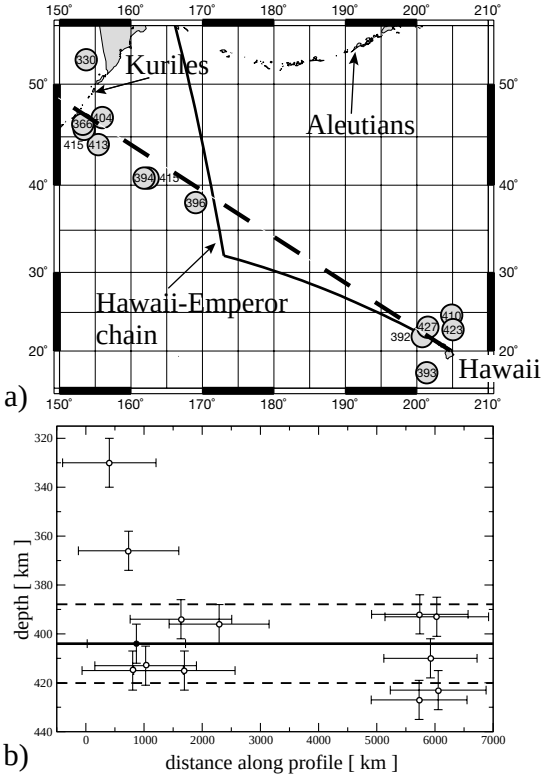

Fig. 5. (a) Reflector depths for the 410-km discontinuity. Depths are given at the *PP* geometric reflection point and range from 330 to 430 km. The solid line marks the strike of the Hawaii–Emperor seamount chain. The dashed line striking NW to SE shows the location of the transect used for the depth profile shown in (b). (b) Depth profile along dashed line shown in (a). The spatial error is due to a conservative $\pm 10°$ backazimuth mislocation estimate projected to the *PP* reflection point. The mean depth of the 410 for all events is 404 ± 16 km shown by the solid and dashed lines, respectively.

this study lacks data in oceanic regions with a presumably simpler upper mantle structure than continental regions.

The depth of the reflector at 410 km depth is shown in Fig. 5. Fig. 5a shows the depth of the reflector at the location of the geometrical bounce point, whereas Fig. 5b shows a profile along the dashed line in Fig. 5a. The mean depth of the reflector is 404 km ± 16 km.

The detections of the 410 form two groups: one near the Kuril subduction zone at the northwestern end of the profile, the other located near Hawaii. Between these two groups a region of ~3600 km along the profile shows no reflections near depths of 400 km, although this region shows clear surface reflections for the same dataset (see Fig. 1 for coverage). Possible reasons for this gap in 410 detections are discussed in the next section.

Except for the two reflection points closest to the Kuril subduction zone ($d = 330$ km and 366 km) the reflection depths are very similar. A blow-up of the region around the Kuril subduction zone is shown in Fig. 6a. The transit of the subducting Pacific plate through the 410 is sampled by one data point assuming the ray theoretical *PP* reflection point that gives a reflector depth of 330 km beneath the Sea of Okhotsk, i.e. ~70 km shallower than the mean depth of 404 km. This shallow depth could be the result of the interaction of the cold subducting slab with the α-to-β phase transformation at 410 km depth. Taking the one shallowest reflector depth measurement as face value and assuming a Clapeyron slope of 2.9 MPa/K [32] for the 410 the elevation corresponds to a temperature difference of ~1000 K. Slab temperatures for 100–130 million year old oceanic lithosphere subducting in the northwest Pacific [33] show temperature differences of 800–1000 K at the 400 km depth level [34,35], in agreement with the temperature difference found here. The elevation of the 410 is much larger than those found elsewhere [5,7], which might be due to averaging between elevated and normal discontinuities in the cap-averaging process [36]. Nonetheless, due to the small aperture of the array and the associated restricted backazimuth resolution the exact location of the anomalous depth reflection

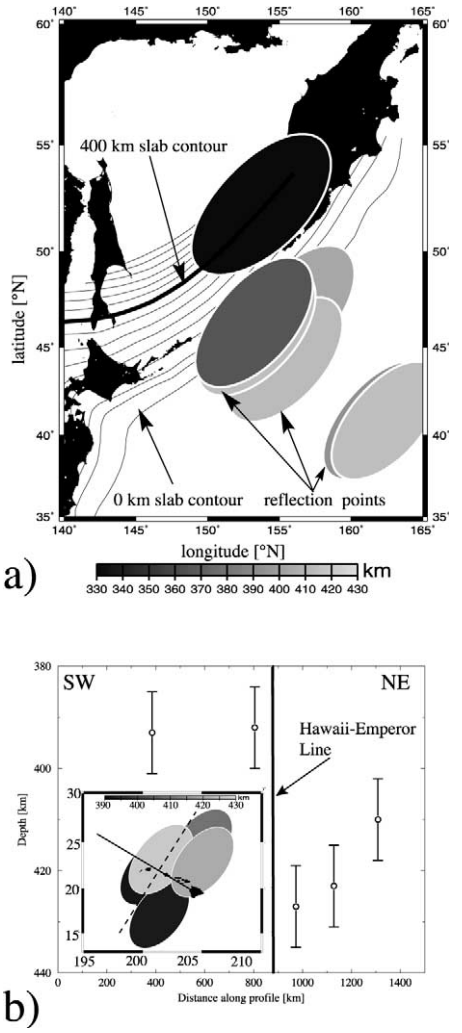

Fig. 6. (a) Location of the reflection points (ellipses) of events showing a reflection from a depth of ~410 km depth near the Kuril subduction zone. The size of the ellipses indicates the approximate size of the inner part of the otherwise saddle shaped Fresnel zone. The thin lines mark slab contours at intervals of 50 km [50]. The thick line marks the 400 km depth contour. Only one bounce point location is able to map the influence of the dipping slab on the discontinuity. This event shows an unusually shallow depth of 330 km. (b) Vertical cross-section for depth of reflection at the 410-km discontinuity along a profile perpendicular to the Hawaiian Chain as indicated by the dashed line in the inlay. The profile covers the five reflections from the tip of the Hawaiian Chain. The strike of the Hawaii–Emperor seamount chain is marked by the solid line. The insert shows the location of the reflection points of our study on the map as ellipses calculated using ray tracing and IASP91.

cannot be determined. The shallow depth of the 410 is unlikely to be an artifact of velocity variations in the upper mantle in the backarc basin beneath the Sea of Okhotsk. To explain the differential travel time anomaly a ~14% faster than IASP91 upper mantle for v_p in the backarc basin beneath the Sea of Okhotsk would be necessary, which is unlikely.

A reflector at about 300 km depth is sometimes observed in the vicinity of subduction zones using *ScS* [10] and *P*-to-*S* conversions [37]. This reflector seems to be related to the hydration of the mantle by the subducted material [10] and might be an alternative explanation for the reflector at 330 km beneath Kamchatka.

The 410 reflections beneath the central Pacific also show some small-scale topography. A cross-section across the Hawaiian Islands is shown in Fig. 6b. The profile (dashed line) runs perpendicular to the Hawaii–Emperor chain from south–west to north–east. We observe ~30 km depth variation along this profile which might be related to the Hawaiian plume. Due to the extensive volcanism at Hawaii we expect the nearby upper mantle to be very heterogeneous at this location, prohibiting a further discussion of reflector topography at this point, due to the uncertainties of the upper mantle velocities. Additionally, the restricted backazimuth resolution of YKA results in a location error that restricts our ability to determine the exact location of the 410 topography.

4.2. The non-detected 660 discontinuity

No reflections from the 660-km discontinuity have been found in our dataset. The non-observation of *P*-wave reflections from the 660 has been noticed previously [11,12]. Both of the previous studies agree that the lack of *P*-wave underside reflections from the 660 cannot be explained by the current Earth models and changes in *P*-wave velocity and density change across the discontinuity are necessary. The short-period dataset used in this study can give lower bounds on the sharpness and upper bounds on the impedance of the discontinuity. Classes of models for the 660 that could explain our data are discussed below.

5. Modeling and discussion

5.1. 410-km discontinuity

The mean depth of the 410 found in this study is 404 ± 16 km and is in good agreement with previous studies [7,38,39]. A long-period global study [7] gives depths for the 410 of 400–405 km south of the Kuriles and of 410–415 km near Hawaii similar to the mean depths for these regions found here. Studies using short-period waves (*pP* and *P′P′*) in different regions showed similar depths of ~410 km (see [38] for data from the Indian Ocean and [39] for continental USA).

The significance of apparent small-scale topography near the Hawaiian Islands and the Kuril subduction zone, discussed in the last section, is difficult to access due to the restricted spatial sampling. Future studies with better spatial sampling are needed before firm conclusions may be drawn concerning this feature.

The lack of reflections from the 410 between the Hawaiian Islands and the bend of the Hawaii–Emperor seamount chain is a prominent feature in Fig. 5. Stacks of long-period waves show a ~30-km depression of the 410 north–west of the Hawaiian Islands that correlates well with the gap in our dataset [7]. A deepening of the 410 is related, among other things, to higher temperatures of the mantle material, but it has been demonstrated that the sharpness of the 410 is temperature dependent [40]. The width of the two-phase field (α and β-spinel phases existing simultaneously) defining the transition thickness narrows for higher temperatures. This would produce a sharper discontinuity for hotter mantle material which should be easier to detect with short-period data, in disagreement with the lack of 410 reflections from this region in our data. The sharpness of the 410 is also controlled by other parameters, e.g. the water content of the material [41]. The β-phase of $(Mg,Fe)_2SiO_4$ can hold significant amounts of H_2O and could be a host for large amounts of H_2O below the depth of 410 km. Mantle Olivine at 410 km depth usually contains $\leq$ 200 ppm H_2O. A content of as little as 500 ppm of H_2O at this depth broadens the transition from olivine to the β-phase from ~7 km to 22 km [41],

thus weakening the short-period $P^{410}P$ reflections. Therefore, our data could be explained by a small water content of the upper mantle material. Because the detailed amount of water stored in the mantle material, the mode of transport of water in the mantle and the possible drying influence of the Hawaiian plume [42] on this mantle region north–west of the Hawaiian Islands are unknown, we do not follow this hypothesis any further.

As discussed before, the reflectivity of the 410 shows lateral differences [26]. This points to an alternative scenario where our detections of the 410 are bright spots of the discontinuity and regions of non-detections are 'normal' discontinuity. The bright spots might be related to special temperature conditions or changing mineral compositions of the mantle (e.g. garnet and iron content [26]).

The sliding-window fk-analysis is unable to resolve the impedance contrast across the reflector directly. Therefore, forward modeling was used. For different one-dimensional models of the discontinuity, synthetic seismograms were computed using the reflectivity method [43]. Two parameters were varied: (i) the thickness of the IASP91 discontinuity and (ii) the impedance change across the discontinuity (due to the reflection origin of $P^{410}P$ we cannot determine velocity and density changes independently). We assume a simple linear gradient of velocity and density for the non-sharp discontinuities. A linear gradient for the growth of the β-phase is not mineralogically realistic and for most peridotites the transformations starts slowly with most of the β-phase forming at the high-pressure end of the transition [26,44]. The exact structure of the phase transition is beyond the scope of this paper, but we might underestimate the reflectivity of the discontinuity.

In Fig. 7, the influence of thickness and impedance on the amplitude of $P^{410}P$ is shown. For the computation of the synthetic seismograms the Earth model IASP91 [27], including attenuation in the upper mantle, was used. In Fig. 7a the gradient thickness of the discontinuity is varied from 0 km (first-order discontinuity) to 18 km assuming the IASP91 velocity model. The $P^{410}P$ phases can be easily detected for the first-order discontinuity but become undetectable for discontinuity

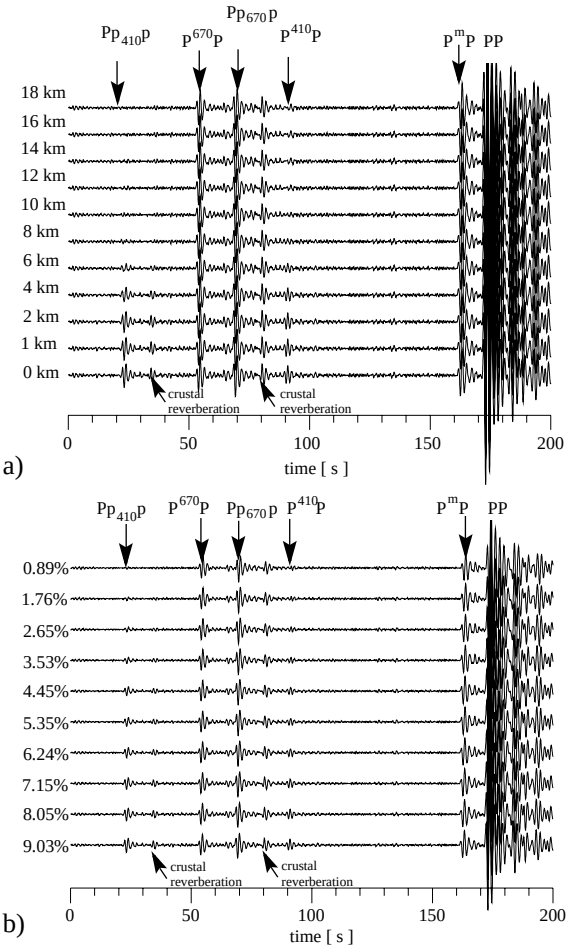

Fig. 7. (a) Synthetic seismograms for variable 410 discontinuity widths using IASP91 as a base model. $P^{410}P$ and the upperside reflection P_{p410p} are only visible if the 410 is sharper than ~6 km. The crustal reverberations are the result of reflections from the Moho at 35 km depth. (b) Variation of the impedance contrast across the 410. The traces show seismograms with impedance contrasts ranging from 0.89% to 9.03%. v_P, v_S and ρ are reduced similarly.

thicknesses larger than 6 km. In Fig. 7b, the impedance contrast is varied reducing S- and P-velocities simultaneously, and the amplitudes of $P^{410}P$ become very small for impedance contrasts smaller than 3.5%.

The synthetic seismograms can be used to set constraints on the discontinuity properties by comparing them with YKA data. In Fig. 8, $P^{410}P$-to-PP amplitude ratios for the synthetic seismograms as function of the discontinuity

thickness are shown. To obtain an upper bound on discontinuity thickness, these amplitude ratios are compared with the mean noise level of the data. The mean noise level is calculated by comparing amplitudes from the precursor time window, i.e. the time window where $P^{410}P$ and $P^{660}P$ are expected, to PP. Detection level tests for the sliding-window fk-analysis show that we are able to detect coherent signals below the noise level [20,23]. The signal must show 50–70% of the noise amplitude to be detectable by sliding-window fk-analysis.

In Fig. 8 the mean noise level in the precursor time window relative to PP for all events of the dataset is marked by the dashed line. The solid lines show the amplitude relative to PP of the minimum detectable signal using YKA and the sliding-window fk-analysis. The smallest signals detectable are in the range of 3.5–5% of the PP amplitude. We measure amplitude ratios of $P^{410}P$ to PP in the synthetic seismograms shown in Fig. 7 which are processed in the same way as the data. By comparing the synthetic signal amplitudes with the mean noise of the data while knowing the detection limit of the sliding-window fk-analysis we are able to set constraints on the thickness and impedance contrast of the 410.

We find that models with 410 transition thicknesses of up to 6 km could be detected in our data, when the IASP91 impedance change is chosen for the discontinuity. This is in agreement with effective widths of 4–8 km of the $\alpha \rightarrow \beta$ transition found by mineral-physical studies [44]. Models with thicknesses less than 6 km show $P^{410}P/PP$ amplitudes above the 50% noise amplitude detection level of the fk-analysis. Models showing a thicker transition for the $\alpha \rightarrow \beta$ phase change show $P^{410}P$ amplitudes well below the detection limit and even a first order discontinuity does not excite precursors well above the 70% noise amplitude detection level of the sliding-window fk-analysis.

Using synthetic seismograms with varying impedance contrasts across a first-order discontinuity we find that a minimum impedance contrast of 6.5% is necessary to produce $P^{410}P$ consistent with the data. IASP91 shows a $\sim$9% impedance contrast across the 410 provided that the PREM

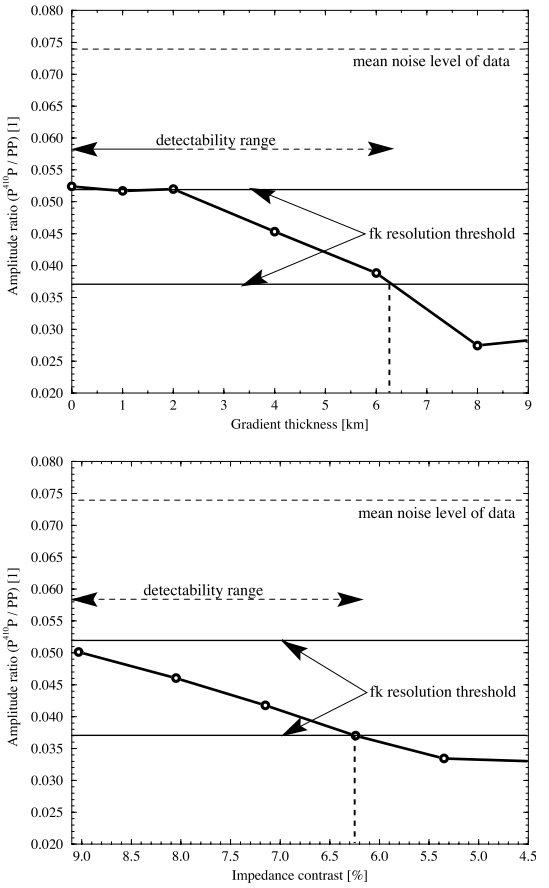

Fig. 8. Synthetic seismogram amplitude ratios of $P^{410}P$ relative to PP versus the gradient thickness and impedance contrast. The synthetic seismograms were processed in the same way as the data prior to taking amplitude measurements. The mean amplitude ratio of PP relative to the noise amplitude of the dataset is marked by the horizontal dashed line. The horizontal solid lines mark the 50–70% detection level of P^dP by the sliding-window fk-analysis. (a) Variation of gradient thickness from a sharp (first-order) discontinuity to a 9-km-thick gradient zone. The amplitude ratios are close to the detection threshold, due to the small velocity change across the 410 in IASP91. (b) Variation of impedance change across the 410 from $\sim$9% to $\sim$1%.

density model is used. Note that also a 9% IASP-like impedance jump produces $P^{410}P$ close to the 70% noise level detection range of sliding-window fk-analysis.

5.2. 660-km discontinuity

Previous results on the P-wave structure of the

660 are quite inconsistent. The 660 is absent in long-period PP stacks [5,11,12], but can be seen in recent short period $P'P'$ studies [45], pP investigations [46], and P-to-S conversions [47]. Nevertheless, the $P'P'$ studies of the 660 often vary strongly over small areas [24,38]. The phase transition γ-spinel → perovskite+magnesiowüstite predicts a sharp discontinuity which should be easily detected by $P'P'$ and PP, but the perovskite forming transition (garnet → perovskite) located at similar depths occurs over a larger depth interval and has a broadening effect on the transition. A broad transition is invisible for short-period waves, but the non-detection of the 660 in long-period investigations cannot be explained by this mechanism. It has been shown that the velocity gradient at the 660 must be as broad as 100 km to explain the missing $P^{660}P$ reflections in 15-s-period P-wave stacks [11]. Such a large depth interval cannot be explained by mineralogical data for the olivine component of the mantle and the missing P reflections are explained by smaller change of bulk modulus [11] or density [12].

Our short-period study imposes constraints on the minimum thickness and the maximum impedance contrast of the 660. For this purpose synthetic reflectivity seismograms for different models of the thickness and the impedance contrast of the 660 have been calculated similar to those for the 410. To give a better estimate of the P-wave structure of the 660 a grid search was performed, computing synthetic seismograms for numerous models of different thickness and impedance contrast. The result of the grid search is shown in Fig. 9, where models producing $P^{660}P$ detectable by the sliding-window fk-analysis are marked by a minus sign, because they are not consistent with the data, whereas models producing undetectable precursors, consistent with the data, are marked by a '+'. Models producing detectable precursors are in disagreement with our data because we cannot detect $P^{660}P$ in the dataset. The model parameters for an IASP91-like 660, that would produce clearly detectable precursors, are shown in the lower right corner. For comparison, the results for the models SF99 [12] and ek1 [11] are marked as circles. Both models of the 660 were developed to explain the absence of $P^{660}P$ from long-period

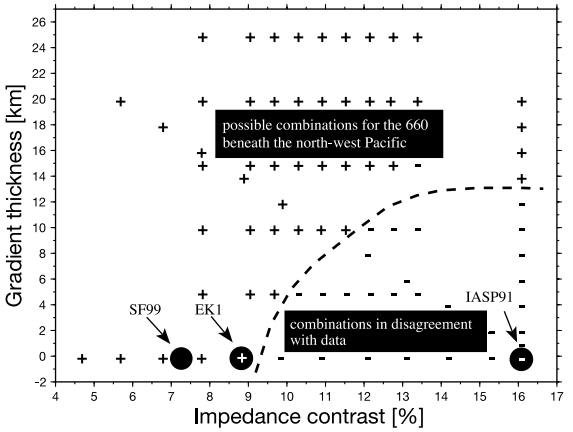

Fig. 9. Grid search for gradient thickness and impedance change across the 660. A '−' denotes a combination producing a detectable precursor; a '+' denotes a combination that would not produce a detectable precursor (in agreement with data). The dashed line marks the estimated boundary between the two fields. For comparison the impedance parameters of three Earth models assuming a sharp discontinuity with varying impedance changes are included. The models SF99 by Flanagan and Shearer [12] and ek1 by Estabrook and Kind [11] are in agreement with our data for the north–western Pacific, whereas IASP91 would produce well observable $P^{660}P$ in disagreement with our study.

P-wave stacks, and are in good agreement with the results of this study. With our short-period data it is possible to set a lower limit of 12 km on the thickness of the discontinuity assuming the IASP91 impedance contrast. This is more than generally accepted by mineralogical studies and other short-period seismological studies [38,48]; however, some long-period SS studies report velocity gradient zones of 20–30 km, which is in agreement with our results [49]. Unfortunately, the trade-off between the thickness and the impedance contrast of the discontinuity makes it impossible to find a unique model of the discontinuity.

6. Conclusions

Using array methods, the 410-km discontinuity was detected beneath the Pacific, using PP underside reflections in a short-period P-wave dataset that affords an improved lateral and vertical res-

olution compared to studies using long-period stacking algorithms. Some indications of strong topography of the 410 in the region of the Hawaiian plume and the Kuril subduction zone have been found, but the paucity of reflection points in these regions and the restricted lateral resolution of the array prohibit a more detailed study. Synthetic experiments and their comparison with data from short-period arrays show that the 410-km discontinuity in the regions where it has been detected with our dataset has to be sharper than 6 km assuming the IASP91 impedance change, or must have an impedance contrast of more than 6.5% assuming a sharp discontinuity. Our models might underestimate the reflectivity of the 410 since we use a linear gradient for the $\alpha \rightarrow \beta$ phase change, which is not realistic. Mineral-physical studies show that the transition from the α- to the β-phase is highly non-linear [44], an effect we do not take into account in our study. In agreement with previous studies we do not detect the 660-km discontinuity with *PP* underside reflections. A parameter search for models explaining the data indicates that the impedance jump at 660 km depth is smaller than 9% for a sharp discontinuity or that the discontinuity is thicker than $\sim$12 km assuming a linear velocity change of 5.8%, as in IASP91. A final model for the thickness and impedance jump of the 660-km discontinuity cannot be given due to trade-offs between the two parameters.

Acknowledgements

We thank the staff, especially Bill Shannon, of the Data Centre of the Geological Survey of Canada (GSC) in Ottawa for the help in retrieving the data, the GSC for use of the YKA Dataset and the German Academic Exchange Service (DAAD) for a travel grant to collect the data. The maps are produced using the GMT software of Wessel and Smith. We thank K. Stammler for his Seismic Handler software. We would like to thank S. Chevrot, J. Gaherty, G. Helffrich, R. van der Hilst and J. Revenaugh for their comments and suggestions that greatly improved this manuscript.***[SK]***

References

[1] L.P. Vinnik, Detection of waves converted from P to SV in the mantle, Earth Planet. Sci. Lett. 15 (1977) 39–45.
[2] S. Chevrot, L. Vinnik, J.-P. Montagner, Global-scale analysis of the mantle Pds phases, J. Geophys. Res. 104 (1999) 20203–20221.
[3] R. Kind, L.P. Vinnik, The upper mantle discontinuities underneath the GRF array from P-to-S converted phases, J. Geophys. 62 (1988) 138–147.
[4] X. Li, R. Kind, K. Priestley, S.V. Sobolev, F. Tilmann, X. Yuan, M. Weber, Mapping the Hawaiian plume conduit with converted seismic waves, Science 405 (2000) 938–941.
[5] P.M. Shearer, Constraints on upper mantle discontinuities from observations of long-period reflected and converted phases, J. Geophys. Res. 96 (1991) 14147–18182.
[6] M.P. Flanagan, P.M. Shearer, Global mapping of topography on transition zone velocity discontinuities by stacking SS precursors, J. Geophys. Res. 103 (1998) 2673–2692.
[7] M.P. Flanagan, P.M. Shearer, A map of topography of the 410-km discontinuity from PP precursors, Geophys. Res. Lett. 26 (1999) 549–552.
[8] J.S. Revenaugh, T.H. Jordan, Mantle layering from ScS reverberations, 1. Waveform inversion of zeroth-order reverberations, J. Geophys. Res. 96 (1991) 19749–19762.
[9] J.S. Revenaugh, T.H. Jordan, Mantle layering from ScS reverberations, 2. The transition zone, J. Geophys. Res. 96 (1991) 19763–19780.
[10] J.S. Revenaugh, T.H. Jordan, Mantle layering from ScS reverberations, 3. The upper mantle, J. Geophys. Res. 96 (1991) 19781–19810.
[11] C.H. Estabrook, R. Kind, The nature of the 660-kilometre upper mantle seismic discontinuities from precursors to the PP phase, Science 274 (1996) 1179–1182.
[12] P.M. Shearer, M.P. Flanagan, Seismic velocity and density jumps across the 410-km and 660-km discontinuities, Science 285 (1999) 1445–1448.
[13] G. Helffrich, Topography of the transition zone seismic discontinuities, Rev. Geophys. 38 (2000) 141–158.
[14] J.L. Cleary, D.W. King, R.A.W. Haddon, P-wave scattering in the Earth's crust and upper mantle, Geophys. J. R. Astron. Soc. 43 (1975) 861–872.
[15] B.A. Bolt, M. O'Neill, A. Qamar, Seismic waves near 100°: is structure in core or upper mantle responsible?, Geophys. J. R. Astron. Soc. 16 (1968) 475–487.
[16] C. Wright, K.J. Muirhead, Longitudinal waves from the Novaya Zemlya nuclear explosion of October 27, 1966, recorded at the Warramunga seismic array, J. Geophys. Res. 74 (1969) 2034–2048.
[17] K.J. Muirhead, R. Datt, The N-th root process applied to seismic array data, Geophys. J. R. Astron. Soc. 47 (1976) 197–210.
[18] H.-P. Harjes, M. Henger, Array Seismologie, Z. Geophys. 21 (1973) 865–905.
[19] K. Aki, P.G. Richards, Quantitative Seismology Theory and Methods, Vol. ii, Freeman and Co., San Francisco, CA, 1980.

[20] S. Rost, M. Weber, A reflector at 200 km depth beneath the Pacific, Geophys. J. Int. 147 (2001) 12–28.
[21] E.J. Kelly, Response of seismic arrays to wide-band signals, Linc. Lab. Techn. Note 1967-30, 1967.
[22] S. Rost, C. Thomas, Array seismology: methods and applications, Rev. Geophys. (2002) in press.
[23] S. Rost, A study of the upper mantle discontinuities in the Pacific using a short period array, Göttinger Beiträge zur Physik No. 7, Duehrkohp und Radicke, Göttingen, 2000.
[24] J.P. Davis, R. Kind, I.S. Sacks, Precursors to P′P′ re-examined using broad-band data, Geophys. J. Int. 99 (1989) 595–604.
[25] J. Revenaugh, S.A. Sipkin, Mantle discontinuity structure beneath China, J. Geophys. Res. 99 (1994) 21911–21928.
[26] J.B. Gaherty, Y. Wang, T.H. Jordan, D.J. Weidner, Testing plausible upper-mantle compositions using fine-scale models of the 410-km discontinuity, Geophys. Res. Lett. 26 (1999) 1641–1644.
[27] B.L.N. Kennett, E.R. Engdahl, Traveltimes for global earthquake location and phase identification, Geophys. J. Int. 105 (1991) 429–465.
[28] F. Neele, H. deRegt, J. VanDecar, Gross errors in upper-mantle discontinuity topography from underside reflection data, Geophys. J. Int. 129 (1997) 194–204.
[29] M. Weber, C.W. Wicks, Reflections from a distant subduction zone, Geophys. Res. Lett. 23 (1996) 1453–1456.
[30] D. Müller, W.R. Roest, J.-Y. Royer, L.M. Gabagan, J.-G. Sclater, Digital isochrones of the world's ocean floor, J. Geophys. Res. 102 (1997) 3211–3214.
[31] R.L. Woodward, G. Masters, Global upper mantle structure from long-period differential travel times, J. Geophys. Res. 96 (1991) 6351–6377.
[32] C.R. Bina, G. Helffrich, Phase transition Clapeyron slopes and transition zone seismic discontinuity topography, J. Geophys. Res. 99 (1994) 15853–15860.
[33] R.D. Jarrard, Relations among subduction parameters, Rev. Geophys. 24 (1986) 217–284.
[34] G. Schubert, D.A. Yuen, D.L. Turcotte, Role of phase transitions in a dynamic mantle, Geophys. J. R. Astron. Soc. 42 (1975) 705–735.
[35] K.C. Creager, T.H. Jordan, Slab penetration into the lower mantle beneath the Mariana and other island arcs of the Northwest Pacific, J. Geophys. Res. 91 (1986) 3573–3589.
[36] F. Niu, S.C. Solomon, P.G. Silver, D. Suetsugu, H. Inoue, Mantle transition-zone structure beneath the South Pacific Superswell and evidence for a mantle plume underlying the Society hotspot, Earth Planet. Sci. Lett. 198 (2002) 371–380.
[37] H.J. Gilbert, A.F. Sheehan, D.A. Wiens, K.G. Dueker, L.M. Dorman, J. Hildebrand, S. Webb, Upper mantle discontinuity structure in the region of the Tonga subduction zone, Geophys. Res. Lett. 28 (2001) 1855–1858.
[38] H.M. Benz, J.E. Vidale, Sharpness of upper mantle discontinuities determined from high-frequency reflections, Nature 365 (1993) 147–150.
[39] T. Melbourne, D. Helmberger, Fine structure of the 410-km discontinuity, J. Geophys. Res. 103 (1998) 10091–10102.
[40] G. Helffrich, C.R. Bina, Frequency dependence of the visibility and depths of mantle seismic discontinuities, Geophys. Res. Lett. 21 (1994) 2613–2616.
[41] B.J. Wood, The effect of H_2O on the 410-kilometre seismic discontinuity, Science 268 (1995) 74–76.
[42] G. Hirth, D.L. Kohlstedt, Water in the oceanic upper mantle; implications for rheology, melt extraction and the evolution of the lithosphere, Earth Planet. Sci. Lett. 144 (1996) 93–108.
[43] G. Müller, The reflectivity method: a tutorial, J. Geophys. 58 (1985) 153–174.
[44] L. Stixrude, Structure and sharpness of phase transitions and mantle discontinuities, J. Geophys. Res. 102 (1997) 14835–14852.
[45] F. Xu, J.E. Vidale, P.S. Earle, H.M. Benz, Mantle discontinuities under southern Africa from precursors to P′P′df, Geophys. Res. Lett. 25 (1998) 571–574.
[46] J.E. Vidale, H.M. Benz, Upper mantle seismic discontinuity and the thermal structure of subduction zones, Nature 356 (1992) 678–683.
[47] N.A. Simmons, H. Gurrola, Multiple seismic discontinuities near the base of the transition zone in the Earth's mantle, Nature 405 (2000) 559–562.
[48] E. Ito, E. Takahashi, Postspinel transformations in the system Mg_2SiO_4-Fe_2SiO_4 and some geophysical implications, J. Geophys. Res. 94 (1989) 10637–10646.
[49] N. Petersen, J. Goßler, R. Kind, K. Stammler, L. Vinnik, Precursors to SS and the structure of the transition zone of the north-western Pacific, Geophys. Res. Lett. 20 (1993) 281–284.
[50] O. Gudmundsson, M. Sambridge, A regionalised upper mantle (RUM) seismic model, J. Geophys. Res. 103 (1998) 7121–7136.
[51] E.R. Engdahl, R.D. vanderHilst, R.P. Buland, Global teleseismic earthquake relocation with improved travel times and procedures for depth determination, Bull. Seism. Soc. Am. 88 (1998) 722–743.